SUPPLEMENTAL MATERIAL

Full-Field Dynamic Characterization of Superhydrophobic Condensation on Biotemplated Nanostructured Surfaces

Emre Ölçeroğlu[†], Chia Y. Hsieh[‡], Md Mahamudur Rahman[†], Kenneth K.S. Lau[‡], and Matthew McCarthy[†]*

[†]Department of Mechanical Engineering and Mechanics, [‡]Department of Chemical and Biological Engineering, Drexel University, 3141 Chestnut St, Philadelphia, PA 19104, USA
*mccarthy@coe.drexel.edu

1 Videos Files

Environmental scanning electron microscopy (ESEM) videos were captured at 0.5 fps using a FEI XL30 SEM operated in wet mode with a chamber pressure of 4.4 Torr. Optical microscopy (OM) videos were captured using a Phantom V210 high-speed camera attached to a Nikon Eclipse LV150 upright microscope at 3 fps. The playback speeds are 60 fps with a field of view 525 μm x 525 μm and total elapsed time of ~12 minutes.

Supporting Movie #1

ESEM imaging with a surface temperature of -1.5°C and S = 1.06, resulting in a low nucleation site density. The playback speed is 1 fps with a field of view of ~ 850 μm x 350 μm oriented at ~15° to the horizontal.

Supporting Movie #2

ESEM imaging with a surface temperature of -2.2°C and S = 1.12, resulting in a high nucleation site density. The playback speed is 2 fps with a field of view in ~ 925 μm x 625 μm oriented at ~30° to the horizontal.

Supporting Movie #3

OM imaging with the chamber ramped to ΔT^{∞}_{sat} = 2.5 °C at a slow ramp rate (Test S_2.5).

Supporting Movie #4

OM imaging with the chamber ramped to ΔT^{∞}_{sat} = 2.5 °C at a fast ramp rate (Test F_2.5).

Supporting Movie #5

OM imaging with the chamber ramped to ΔT^{∞}_{sat} = 6.5 °C at a slow ramp rate (Test S_6.5).

Supporting Movie #6

OM imaging with the chamber ramped to ΔT^{∞}_{sat} = 6.5 °C at a fast ramp rate (Test S_6.5).

Supporting Movie #7

Extended testing at ΔT^{∞}_{sat} = 2.5 °C after 20 hours of operation.

Supporting Movie #8

Extended testing at ΔT^{∞}_{sat} = 2.5 °C after 24 hours of operation.

2 Fabrication

2.1 The Tobacco mosaic virus and Biotemplated Nanofabrication

The *Tobacco mosaic virus* (TMV) is a benign cylindrical plant virus. It has an 18 nm outer diameter and 300 nm length[S1,S2]. The TMV used in this work is the TMV1cys, an engineered mutant of the wild-type virus containing a cysteine residue on the outer surface of its coat proteins[S3]. This results in enhanced binding properties, allowing for near-vertical assembly and metallization onto various substrates, resulting in highly textured three-dimensional metal-coated nanostructures[S4]. The TMV solutions used in this study are prepared through the inoculation of tobacco plants (*Nicotiana tabacum cultivar Xanthi*). When seedlings are 3-4 weeks they are infected with the TMV by rubbing existing solutions onto the leaves. The infected tobacco grows for 2-3 weeks, and TMV replicates during the infection process. The leaves are collected and stored at -20 °C until the purification process begins. The TMV is extracted by blending the plant material using a standard kitchen blender. A series of chemical and centrifuging steps are then used to purify and separate the TMV from the rest of the plant material. The purified TMV is finally diluted to 0.1 g/L using 0.1M sodium phosphate buffer. The room-temperature solution-based biotemplating process is shown in Figure S1a. Gold-coated silicon chips are submerged in 0.1 g/L TMV solutions at room temperature for 18-24 hours while the virus particles self-assemble onto the surface. After viral assembly, the chips are placed in a 1:15 mixture of 10 mM sodium (II) tetrachloropalladate (Na2PdCl4) and 0.1M sodium phosphate buffer for 2-3 hours. Palladium nanoclusters are formed onto the TMV surface during this step, which act as a catalyst for the final electroless nickel plating step in a 1:1 mixture of nickel solution (0.1M nickel (II) chloride (NiCl2), 0.15M sodium tetraborate (Na2B4O7), 0.25M glycine, and 0.5M dimethylamine borane (DMAB)) and distilled water for 3-5 minutes. Figure S1b shows SEM images at three magnifications of the resulting nickel nanostructured surfaces.

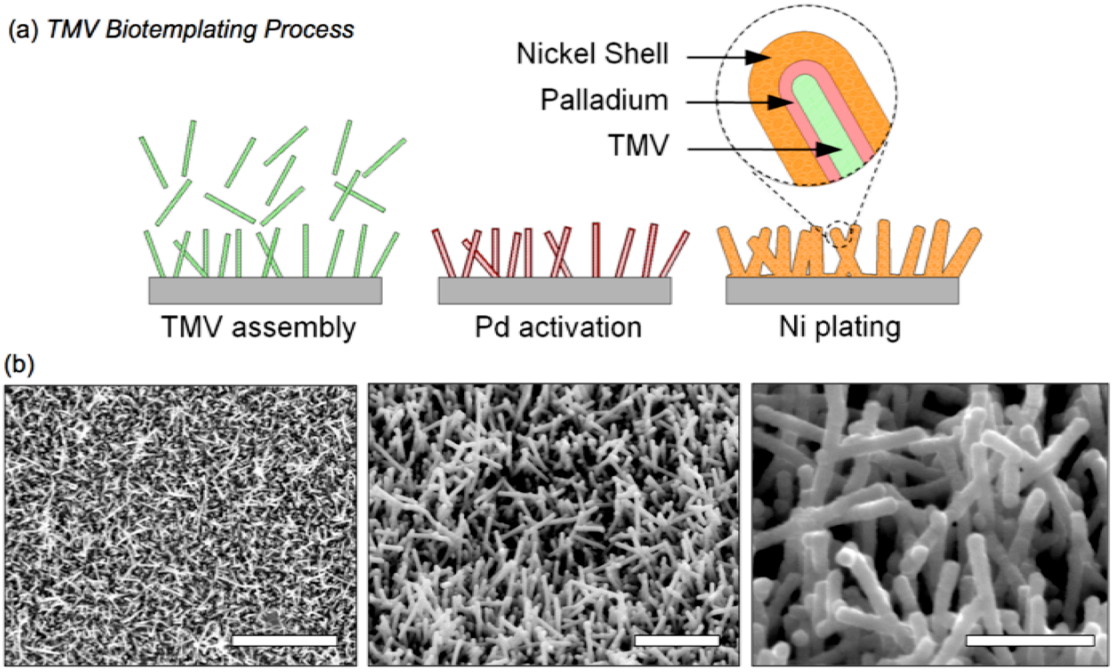

Figure S1: Biotemplated nanofabrication using the *Tobacco mosaic virus* (TMV) showing (a) the three-step solution-based room-temperature process and (b) SEM imaging of the resulting nanostructured coating at various magnifications. Scale bars are 5 μm, 2 μm, and 1 μm.

2.2 Initiated Chemical Vapor Deposition (iCVD)

The iCVD reactor setup used in this work has been described previously and is shown in Figure S2[S5-S7]. For the specific case of performing iCVD of PTFE films here, samples were placed on an aluminum stage cooled by a recirculating chiller set at 20 °C. Then, hexafluoropropylene oxide (HFPO) of 5 sccm and nonafluorobutanesulfonyl fluoride (FBSF) of 1 sccm were introduced as gas into the iCVD chamber and a reactor pressure of 300 mtorr was maintained. The phosphor bronze filament wire array was then heated to 300 °C to initiate the iCVD polymerization and deposition. The thickness of the PTFE film was monitored *in situ* using an interferometry system that tracks the deposition rate in real-time as the deposition occurs. This system is equipped with a 633-nm HeNe laser (JDS Uniphase) and it reaches into the reaction zone through a glass window on top of the chamber[S8]. After ~10 nm PTFE deposition, samples were taken out from the iCVD reactor chamber for further analysis without any post-processing. HFPO gas was purchased from Oakwood Chemical and used as received. FBSF (90+%) was obtained from Alfa Aesar and used without further purification. The phosphor bronze filament wire was supplied by The Instrument Workshop Co.

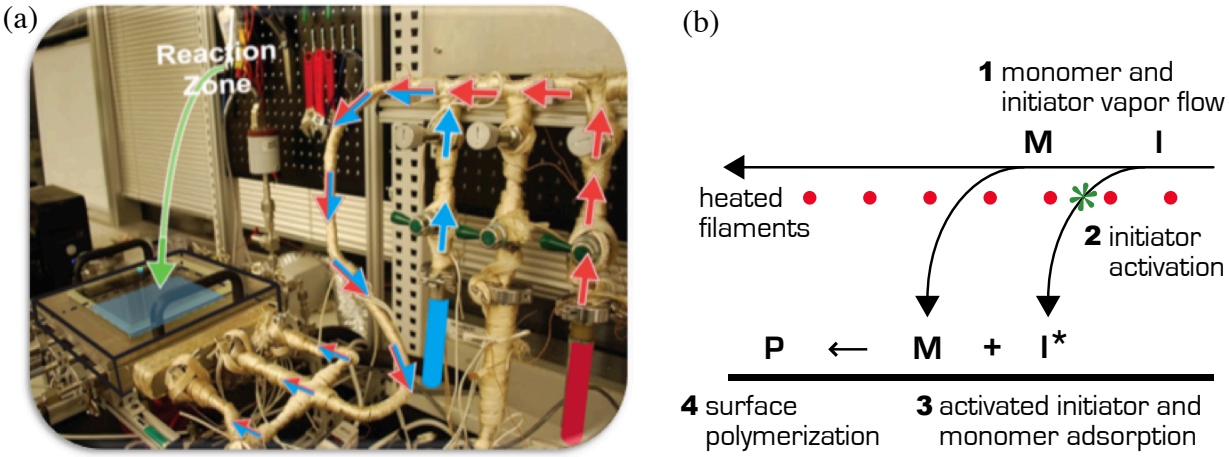

Figure S2. Initiated chemical vapor deposition, showing (a) the reactor setup, consisting of a vapor delivery module, the main reactor chamber, and a mild vacuum pump system. (b) The iCVD process, showing a one-step polymerization and polymer coating formation from starting monomer and initiator vapor precursors.

3 Experimental Methods

3.1 Environmental Scanning Electron Microscopy (ESEM)

A FEI XL30 ESEM is used to investigate the wetting morphology and contact angle behavior of condensate droplets. A 500 μm lower aperture was coupled with a 1000 μm pressure limiting aperture (PLA) for larger field of view with a beam potential limited to 20kV to avoid heating effects[S9]. A gaseous secondary electron detector (GSED) was used for better imaging through the vapor inside the chamber. The samples are placed on a 75° inclined fixture which is attached to the peltier stage. A thin layer of thermal grease was used between both contact areas to ensure minimal temperature drop throughout the conduction path from the peltier stage to the sample. Sample was cooled down to -0.5 ± 1.5 °C at 4.4 ± 0.5 Torr and allowed to equilibrate for 5-10 minutes. After equilibrium, sample temperature was brought down by 1 ± 1.5 °C until condensation began. The apparent droplet contact angle as a function of radius was evaluated by analyzing 60 individual droplets of various sizes using *ImageJ* analysis software (Figure 2). The height and radius of each droplet were measured (Figure 1d), and the contact angle calculated as

$$\theta = \sin^{-1}\left(\frac{H-R}{R}\right)+\frac{\pi}{2}. \qquad \text{(S1)}$$

Use of this geometrical expression to show the relationship between droplet morphology and contact angle has been suggested and confirmed by Enright *et al.*[S10]. The uncertainty of this measurement is estimated to ±5% based on image resolution and repeatability of the technique.

3.2 Optical Microscopy (OM) Experimental Apparatus

The experimental setup used in this work is shown in Figure S3. An aluminum cooling block and a humidity / temperature sensor (Rotronic HC2-S) are packaged inside an acrylic chamber. The chamber has an inlet for humid/dry N_2 and the enclosure with cooling water circulating between the cold plate and a constant temperature bath (Thermo Scientific Haake ARCTIC SC150 A25). The sample is viewed from above using a Nikon Eclipse LV150 upright optical microscope fitted with a Phantom V210 high-speed 1Mpixel CCD camera, using a 20x magnification with a field of view of 525 ± 1 x 525 ± 1 μm. The chamber temperature and relative humidity (RH) were recorded with an accuracy of ±0.1°C and ±0.8 RH%. Stage temperature was monitored by a T-type thermocouple placed right underneath the sample through a hole drilled into the cold plate. The difference between the saturation temperature of the chamber and the sample temperature (ΔT^{∞}_{sat}) was calculated and monitored in LabView.

Samples were cleaned with IPA, rinsed with DI water, dried with N_2, and dehydrated at 100°C for 10 minutes. The samples are then fixed to the cold plate using thermal grease to minimize thermal resistance. Dry N_2 was constantly pumped into the chamber to bring the enclosure RH down to ~1%. When the chamber reached dry condition, the sample temperature was set to the desired value (see Table 1) by adjusting the constant temperature bath. A three-way valve was then used to switch from dry N_2 to humid N_2 sparged through a bath of water at ambient temperature. The steady state conditions were attained at two different ramp rates, denoted as "fast" and "slow" for both values of steady state ΔT^{∞}_{sat} by throttling the N_2 using a flow control valve. Figure S4 shows the resulting dynamic thermal loading for the four tests considered in this work. Videos of the condensation process are recorded at 3 fps starting from before the initial nucleation, running for approximately 12 minutes.

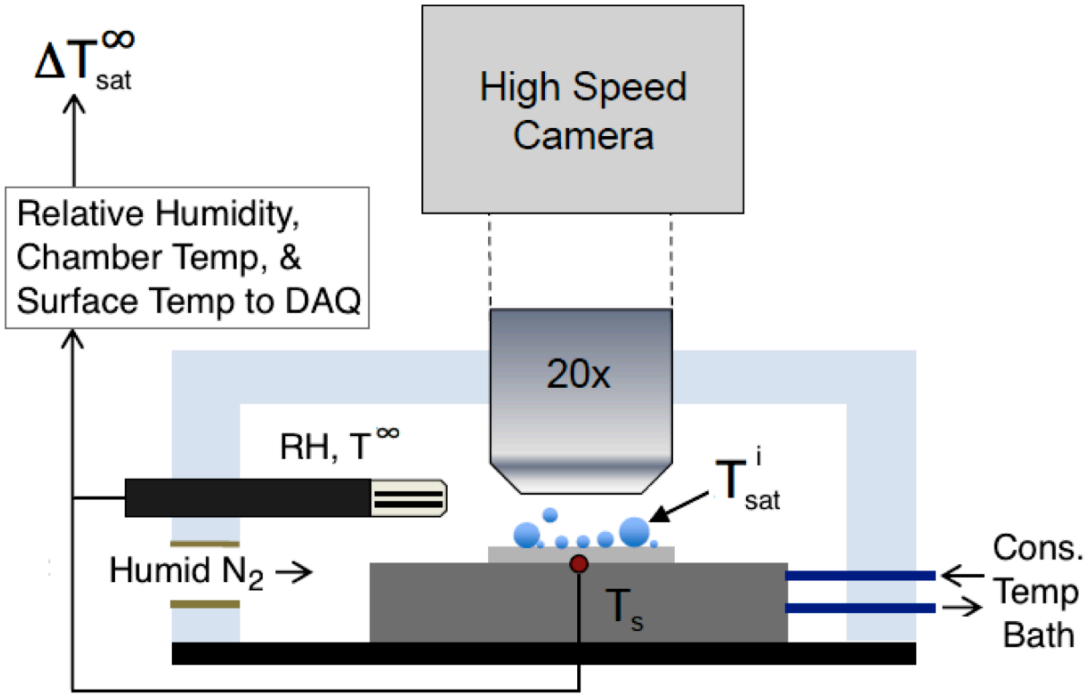

Figure S3: Experimental apparatus for characterization of superhydrophobic condensation.

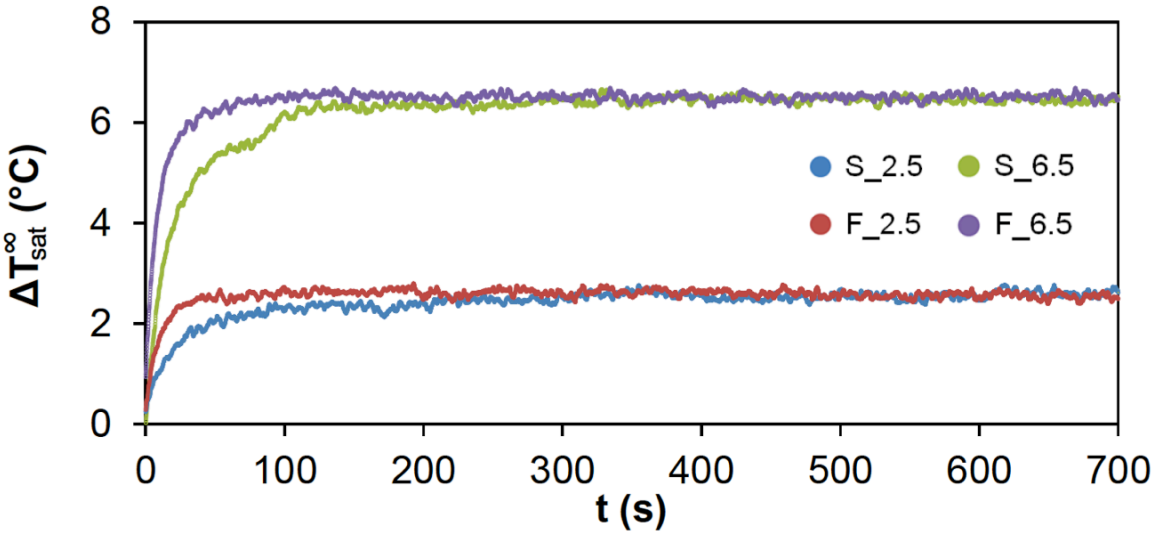

Figure S4: Saturation temperature difference within the chamber as a function of time for the test conditions listed in Table 1, showing fast and slow ramping to $\Delta T^{\infty}_{sat} = 2.5°C$ and $\Delta T^{\infty}_{sat} = 6.5°C$.

3.3 Image Processing

The captured videos are decomposed into separate image files of each individual frame, with a time-step between frames of 0.33 s. These individual frames are then fed into a custom-built droplet detection algorithm in MATLAB to identify the location of every droplet in each frame and measure it's diameter. The algorithm is based on the Hough transform method[S11-S13] and modified to effectively and efficiently detect droplets of different sizes as well as droplets in close proximity to one another. To improve the accuracy of the detection algorithm, movies are recorded at high contrasts and a simple pre-processing step is used to convert the images from gray-scale to black-and-white. Figure S5 shows a set of randomly selected frames from the "ΔT^{∞}_{sat} = 2.5°C slow ramp" test at time intervals from 35s to 500s. The application of the algorithm can be seen, where red circles are superimposed over detected droplets. The optimized algorithm yielded accurate detection results with only a small amount of "undetected droplets" remaining. By manually inspecting these images (and numerous other frames), it has been shown that the algorithm detects 95%-98% of the droplets across all stages of the experiments. The uncertainty in number of detected droplets is therefore taken to be ± 3.5%. The algorithm has been used to detect droplets with a diameter as small as 2.5 μm, and the uncertainty in diameter is estimated to be ±0.5 μm based on pixel size (1 pixel = ~1micron) and scatter in the data.

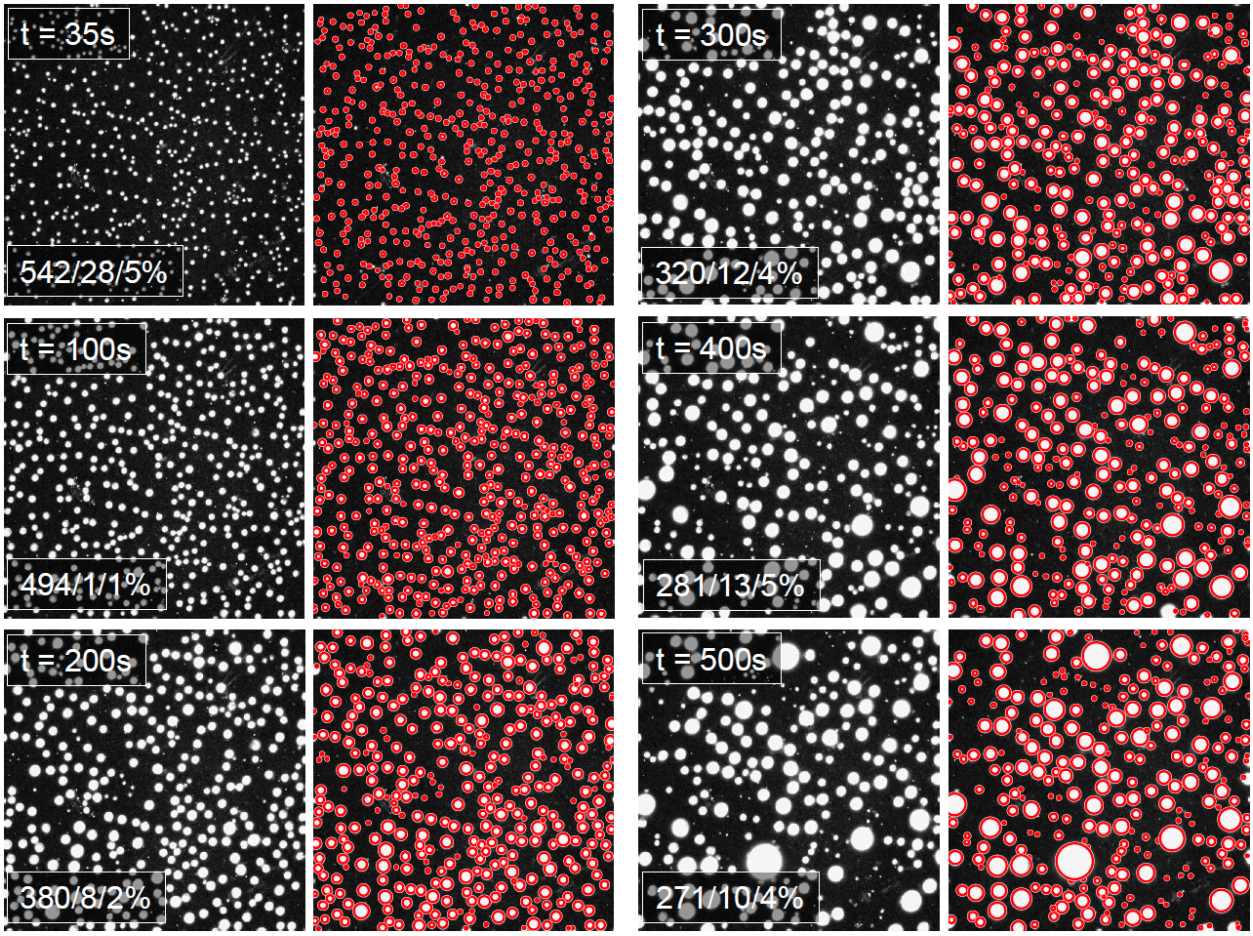

Figure S5: Full-field image processing of droplet nucleation, growth, coalescence, and ejection. Inset showing number of successfully detected droplets/missed droplets/error percentage values.

3.4 Droplet Dynamics and Size Distribution

Figure S6 shows the droplet size distributions for each of the four test conditions, including the dynamic variation is size distributions, as well as the steady state values.

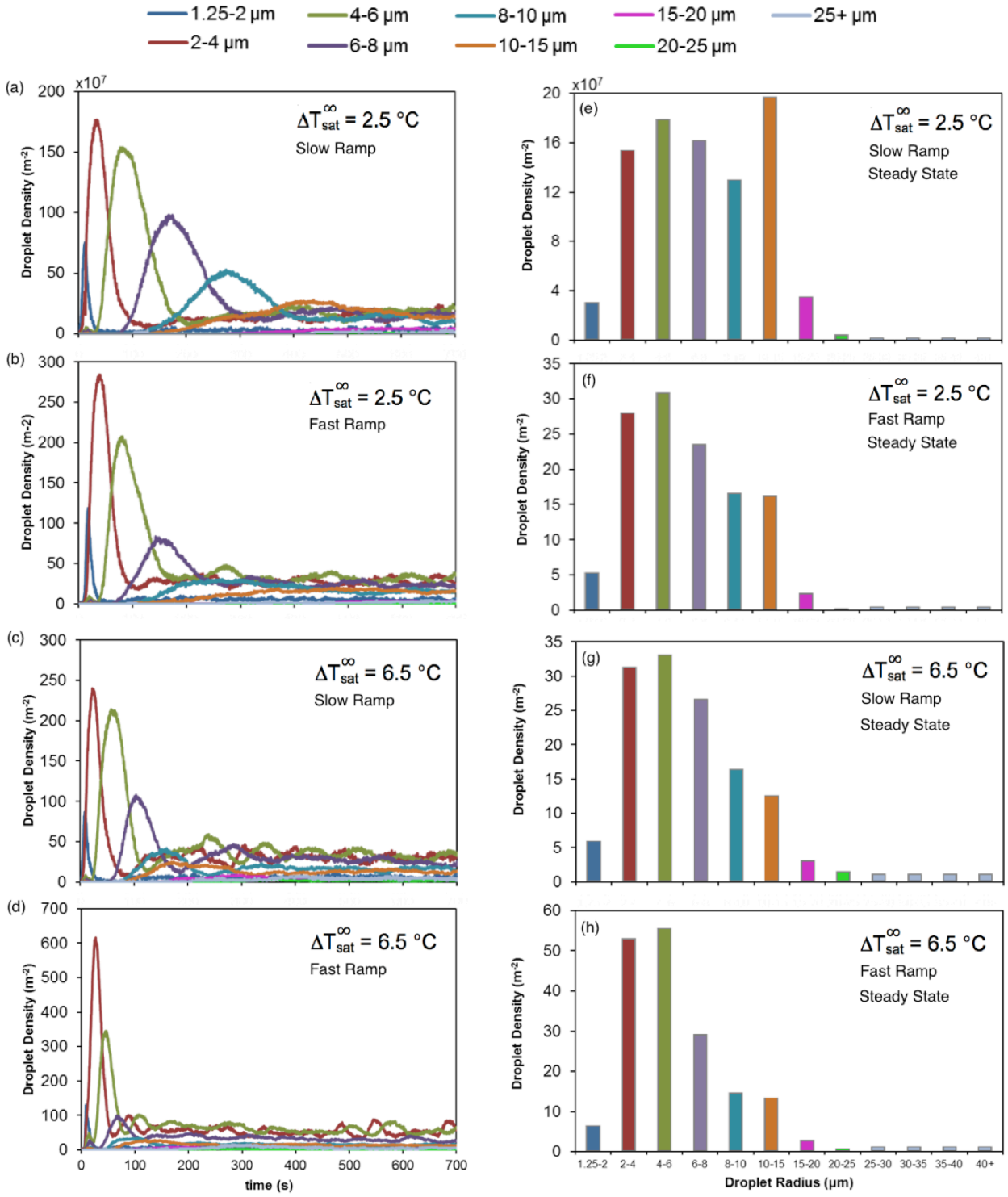

Figure S6: (a) Dynamic droplet size distribution and (b) the steady state values (averaged over times t > 300s) for all four test conditions.

4 Droplet Growth Rate and Surface Heat Flux

4.1 Thermal Circuit Modeling

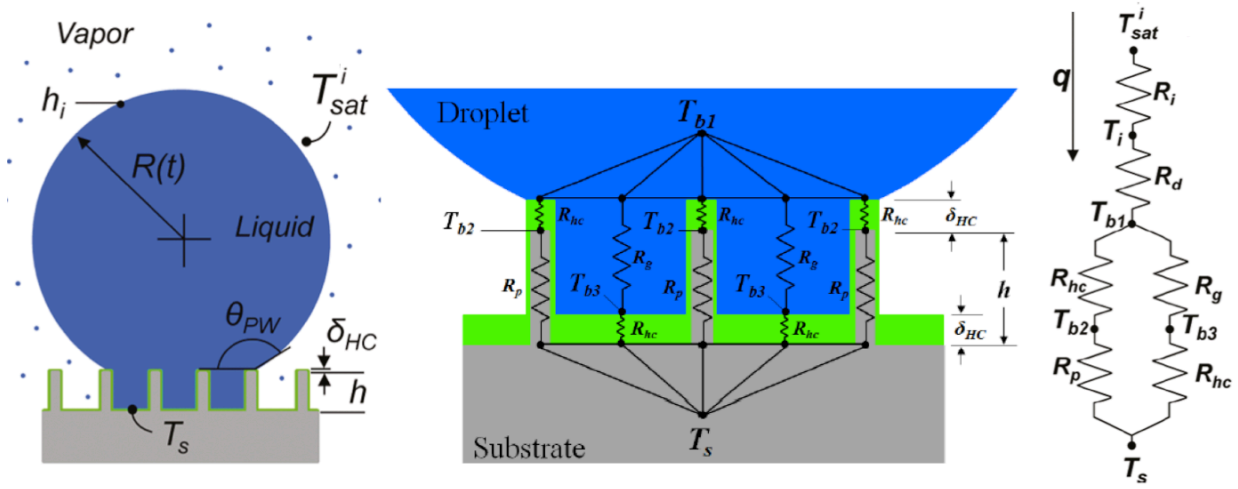

Figure S7: Schematic representation of the thermal resistance network through a "partially-wetting" microscale droplet on a superhydrophobic nanostructured surface coated with a thin hydrophobic coating[S15]. Reprinted with permission from *ACS*, copyright 2012.

A closed-form thermal circuit model was used in this work to validate experiments as well as evaluate the interfacial saturation temperature difference. This model was presented by Carey[S14] and modified for superhydrophobic condensation on ordered arrays of micro/nano-scale posts by Miljkovic *et al.*[S15]. Figure S7 shows the schematic representation of the thermal circuit for a singular droplet in a partially wetted state on a superhydrophobic micro/nanostructured surface. This circuit accounts for resistances due to droplet curvature, condensation, conduction through the droplet, and conduction through the wetted hydrophobic nanostructures underneath the droplet.

Using this thermal circuit the heat transfer rate through a single droplet can be evaluated as

$$\dot{q}_{drop,model} = \frac{\pi R^2 \left(\Delta T^i_{sat} - \frac{2T^i_{sat}\sigma}{R h_{fg} \rho_W} \right)}{\frac{1}{2h_i(1-\cos\theta)} + \frac{R\theta}{4k_W \sin\theta} + \frac{1}{k_{HC}\sin^2\theta}\left\{ \frac{k_p \varphi}{\delta_{HC}k_P + hk_{HC}} + \frac{k_W(1-\varphi)}{\delta_{HC}k_W + hk_{HC}} \right\}^{-1}} \tag{S2}$$

$$h_i = \frac{2\alpha}{2-\alpha} \frac{1}{\sqrt{2\pi R_g T_s}} \frac{{h_{fg}}^2}{v_g T_s} \tag{S3}$$

where h_i is the condensation heat transfer coefficient ($\alpha = 0.9$), σ is the surface tension, and ν_g and R_g are the specific volume and universal gas constant of the water vapor, respectively. The nanostructure height is given by h, the thickness of the hydrophobic coating is δ_{HC}, the solid fraction of the post array is φ, and the thermal conductivity of the water, nanostructures, and hydrophobic coating are given by k_W, k_P, and k_{HC}, respectively. Setting Equation S2 equal to

Equation 5, making simplifying assumptions regarding the rate at which contact angle varies, and discretizing with respect to time, Equation S4 was derived for droplet growth rate[S15].

$$R_{t+\Delta t} = R_t + \left[\frac{\Delta t}{\rho_W h_{fg}(1-\cos\theta)^2(2+\cos\theta)}\right] \times \left[\frac{\Delta T_{sat}^i - \frac{2T_{sat}^i \sigma}{R_t h_{fg} \rho_W}}{\frac{1}{2h_i(1-\cos\theta)} + \frac{R_t\theta}{4k_W \sin\theta} + \frac{1}{k_{HC}\sin^2\theta}\left\{\frac{k_p\varphi}{\delta_{HC}k_P + hk_{HC}} + \frac{k_W(1-\varphi)}{\delta_{HC}k_W + hk_{HC}}\right\}^{-1}}\right] \quad \text{(S4)}$$

Figure S8 and Figure 4 show the growth rates for over 40 droplets measured using the experimental techniques presented here. They are plotted against Equation S4, which is solved numerically using a time step of Δt = 100 ms, where the contact angle is evaluated using Equation 1 at each time step. The material properties of the fabricated surfaces were k_P = 90 W/mK and k_{HC} = 0.25 W/mK. Nanostructure height and PTFE thickness were estimated using SEM to be ~1 μm and ~10 nm, respectively, while the solid fraction has been determined elsewhere to be φ = 0.03[S16]. The interfacial saturation temperature differences (ΔT^{i}_{sat}) listed in Table 1 are determined using these curves fits, were ΔT^{i}_{sat} = 0.011 ±0.002°C and ΔT^{i}_{sat} = 0.017 ±0.002°C show excellent agreement with the data collected at ΔT^{∞}_{sat} = 2.5°C and ΔT^{∞}_{sat} = 6.5°C, respectively. As expected, the presence of non-condensable gases greatly reduces the saturation temperature difference near the interface relative to that measured in the chamber.

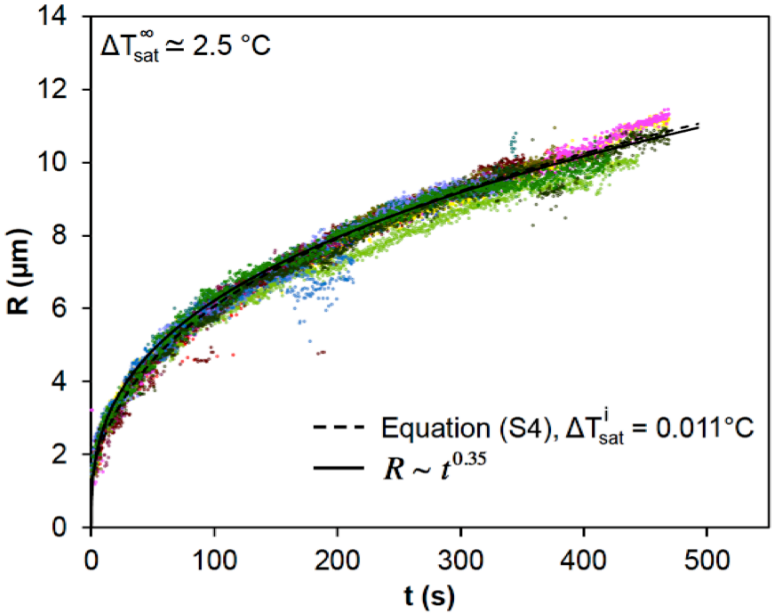

Figure S8: Droplet growth rate at ΔT^{∞}_{sat} = 2.5°C. Showing radius as a function of time for 17 separate droplets (from both the fast and slow ramp tests), plotted against the thermal circuit model prediction from Equation S4 (dashed line) and a power law fit from Equation 2 (solid line).

The experimental technique developed in this work using optical microscopy and droplet image tracking, has been validated against modeling predictions. Surface heat flux was modeled using the predictions of heat transfer rate for individual droplets based on thermal circuit modeling (Equation S2), combined with predictions of droplet size distributions. The total surface heat flux is estimated by Miljkovic *et al.*[S17], for partially wetted droplets undergoing jumping-mode condensation on superhydrophobic nanostructured surfaces with dynamic contact angles, as:

$$\dot{Q}''_{Model} = \int_{R_{\min}}^{Lc/2} \dot{q}_{drop\ Model}(R)\, n_d(R)\, dR \tag{S5}$$

where n_d is the dynamic droplet size distribution and R_{min} is given as the critical radius of nucleation as predicted by classical nucleation theory[S14]. This model builds on the previous work by Abu-Orabi[S18] and Kim *et al.*[S19], including all relevant thermal resistances and the effects of large contact angles. The dynamic droplet distribution, n_d, is found by numerically solving the differential equation

$$\frac{dn_d}{dR} + \frac{1}{G_{pw}}\frac{dG_{pw}}{dR} n_d = 0 \tag{S6}$$

where G_{pw} is the analytically derived droplet growth rate, and the predicted heat transfer coefficient is therefore given by:

$$h_{C,Model} = \dot{Q}''_{Model} / \Delta T_{sat}^{i} \tag{S7}$$

Equations (S5-S7) are solved numerically using the geometric parameters and material properties listed above and plotted against the experimentally measure heat flux and heat transfer coefficient in Figure 8 and Figure 9, showing strong agreement. Complete details of the modeling approach are provided by Miljkovic *et al.*[S17].

4.2 Experimental Heat Flux Calculation

The total surface heat flux measured in this work is calculated using Equation 3 where the individual heat transfer rate for each dropet in each frame is given by Equation 5. The differential terms in Equation 5, dθ/dR and dR/dt, are evaluated by differentiation of Equation 1 and Equation 2, resulting in

$$\frac{d\theta}{dR} = \frac{R_p}{R^2\sqrt{1-\left(R_P/R\right)^2}} \tag{S8}$$

$$\frac{dR}{dt} = B^{1/C} C R^{(1-1/C)} \tag{S9}$$

where R_p, B, and C are the empirically derived terms described in the previous sections.

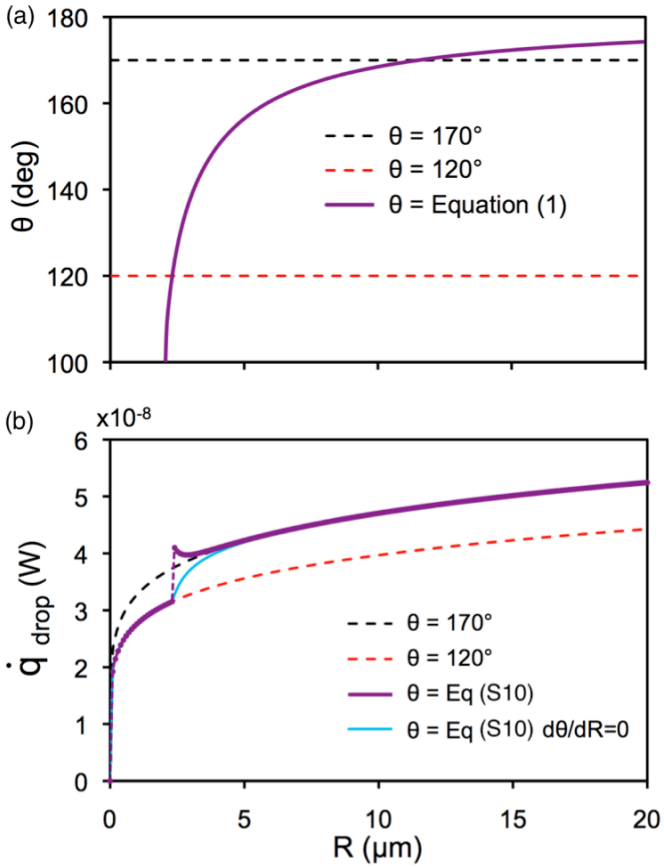

Figure S9: Droplet (a) contact angle and (b) heat transfer rate as a function of radius.

Figure S9 shows the contact angle and heat transfer rate calculated for each droplet as a function of radius, based on the experimentally measured growth rates. The minimum observed contact angle was consistent the intrinsic advancing contact angle of the PTFE coating ($\theta_{PTFE,\,a} = 120°$), and the maximum observable contact angle was consistent with the macroscopically measured value of ($\theta_{macro} = 170°$). As such, the droplet contact angle was taken to be a piecewise function of the form

$$\theta(R) = \begin{cases} \theta_{\min} = 120^{\circ} \\ \theta = \cos^{-1}\left(\frac{R_P}{R}\right) + \frac{\pi}{2} \quad (Eq\,1) \\ \theta_{\max} = 170^{\circ} \end{cases} \tag{S10}$$

where the dynamic contact angle varies between 120°-170° with the form given by Equation (1). Figure S9b shows the heat transfer rate of an individual droplet as a function of radius (Equation 5) where contact angle is given by Equation S10 (purple curve). It can be seen that the heat transfer rate varies between the constant contact angle predictions, with a discontinuity around $R = 2.3$ μm. This discontinuity is an artificial by-product of the sharp change in dθ/dR at the transition from the minimum contact angle to the dynamic contact angle (given by Equation (S10)), and represents an overestimate of heat transfer in this region. Droplet heat transfer rate is also plotted assuming the dθ/dR term in Equation 5 is negligible (blue curve),

representing an underestimate by definition. It can be shown the average variation between these two curves is ~12% over the range of radii of R = 2.3 – 3.5 μm. While, droplets in this size range account for <20% of the total droplets on the surface at any given moment (Figure S6). This leads to the conclusion that the difference between these two approaches (one an over estimate, one an underestimate) results in variations in the total surface heat flux of ~2%. Based on this negligible error, the heat transfer rate for each detected droplet was calculated based on Equations 5 and S10 (purple curve).

4.2.1 Error from Minimum Detectable Droplet Sizes

The minimal detected droplet radius was R_{min} ~1.25 μm, meaning that any heat transferred prior to the droplet reaching this size is not being accounted. The resulting error being introduced by this has been estimated below using two methods and plotted relative to the coalescence length in Figure S10. The first uses the experimentally measured droplet growth rates, and the second uses previously derived analytical approximations of condensation heat transfer.

Method #1:

For a single droplet, the total heat transferred over a time span $\Delta t = (t_f - t_i)$ is given by

$$q_{drop} = \int_{t_i}^{t_f} \dot{q}_{drop}(R)\, dt \tag{S11}$$

where $\dot{q}_{drop}(R)$ is the droplet heat transfer rate as a function of radius, as given by Equation 5. Solving the expression for the experimentally measured growth rates (Equation 2) in terms of time yields $t = (R/B)^{1/C}$ (where B is the empirically derived constant). This is then plugged into Equation S11, yielding the total heat transferred to a droplet as a function of its initial and final radii

$$q_{drop} = \int_{(R_i/B)^{1/C}}^{(R_f/B)^{1/C}} \dot{q}_{drop}(R = Bt^C)\, dt \; = f(R_f, R_i, \theta) \tag{S12}$$

where R_f and R_i are the final and initial droplet radii corresponding to the time span. Assuming negligible changes in contact angle, the resulting error associated with the minimum detectable radius for a single droplet can therefore be found to be

$$\Delta_{Method\,1} = \frac{q_{drop\,ideal} - q_{drop\,measured}}{q_{drop\,ideal}} = \left(\frac{2R_{\min}}{L_C}\right)^3 \tag{S13}$$

where $q_{drop\,ideal}$ is evaluated using $R_i = 0$, $q_{drop\,measured}$ is evaluated using $R_i = R_{min}$, and the final droplet size is given by half of the coalescence length for both.

Method #2:

Using the modeling approach reported by Miljkovic *et al.*[S17] (and briefly described above), the error associated with the minimal detectable droplet size has been approximated using a second method. The error for the entire surface is given by:

$$\Delta_{Method\ 2} = \frac{\dot{Q}''_{Model,ideal} - \dot{Q}''_{Model,observed}}{\dot{Q}''_{Model,ideal}} = \frac{\int_{R=0}^{Lc/2} \dot{q}_{drop\ Model}(R)\, n_d(R) dR - \int_{R_{min}=1.25\mu m}^{Lc/2} \dot{q}_{drop\ Model}(R)\, n_d(R) dR}{\int_{R=0}^{Lc/2} \dot{q}_{drop\ Model}(R)\, n_d(R) dR} \quad \text{(S14)}$$

where the individual droplet heat transfer rates are given by Equation S2, the dynamic droplet distribution is solved numerically from Equation S5, and the integrals are evaluated from $R = 0$ to half the coalescence length for the ideal case, and from $R = R_{min} = 1.25$ μm to half the coalescence length for the "observed" experimental minimum. The percent error for both approaches are shown in Figure S10. This error in is less than 1% for the minimum detectable radius ($R_{min} = 1.25$ μm) and the average coalescence length ($L_c = 12$ μm) reported here, and varies from ~0.2 - 5% over the range of conditions used in this work. Additionally, over 85% of the experimentally measured coalescence lengths are above 9 μm, with associated errors falling below 2%, suggesting that this effect has a minimal impact on overall experimental accuracy due to the short duration over which the droplet is below R_{min}.

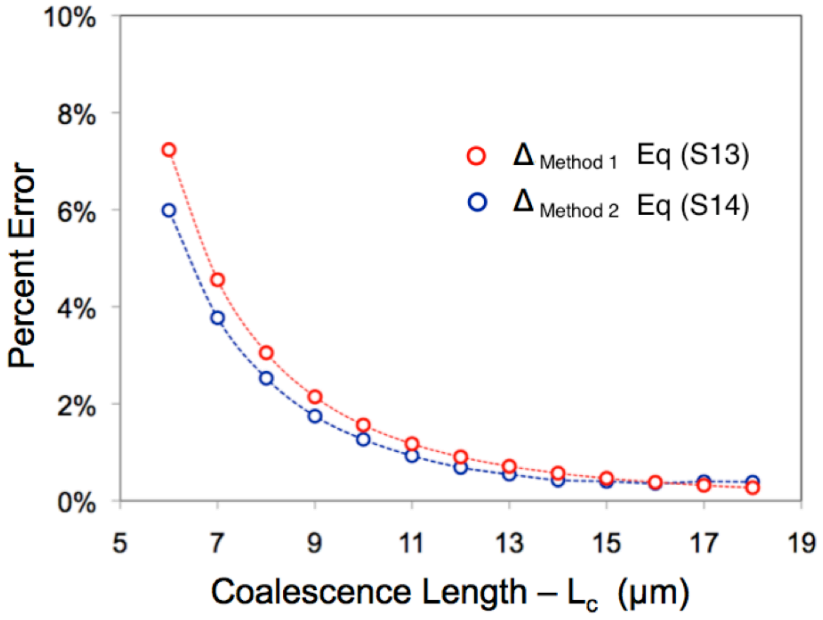

Figure S10: Error estimate associated with the minimum detectable radius as a function of L_c.

5 Extended Operation

Multiple virus-structured iCVD functionalized superhydrophobic surfaces were tested for extended periods, showing sustained jumping-mode condensation for over 24 hrs of operation (Figure S11). See supporting movie files #7 and #8 for videos after 20 hours and 24 hours.

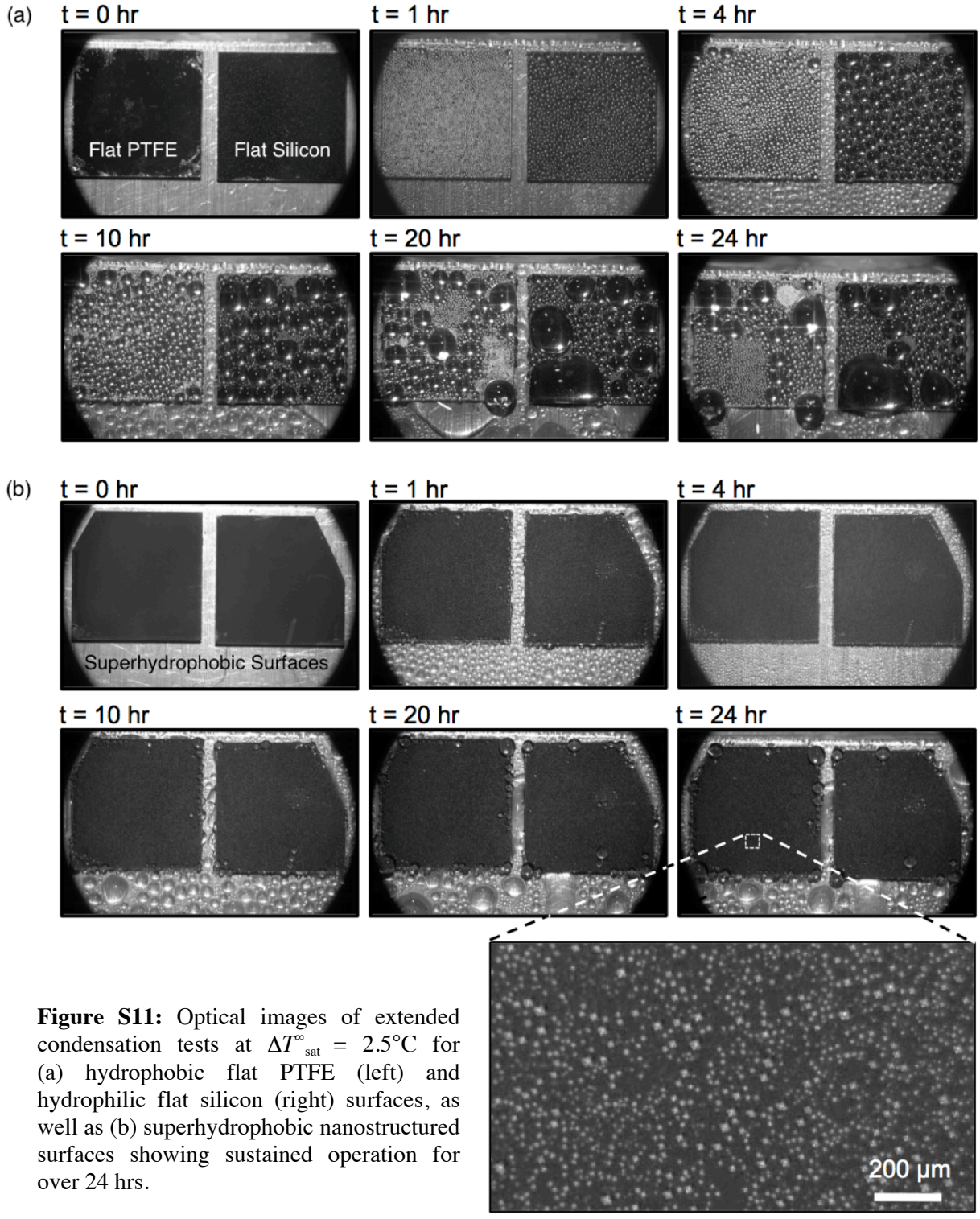

Figure S11: Optical images of extended condensation tests at ΔT^{∞}_{sat} = 2.5°C for (a) hydrophobic flat PTFE (left) and hydrophilic flat silicon (right) surfaces, as well as (b) superhydrophobic nanostructured surfaces showing sustained operation for over 24 hrs.

6 Uncertainty Analysis

6.1 Droplet Density, Size, and Distribution

The basic measurements made using the reported technique are droplet radius (R), the number of droplets detected in each frame (n), and the field of view area (A). Using the estimated uncertainties of these measured values (described above), the uncertainties in nucleation site density, average droplet radius, and coalescence length are calculated using the propagation of errors as

$$\left(\frac{\Delta N}{N}\right)^2 = \left(\frac{\Delta n}{n}\right)^2 + \left(\frac{\Delta A}{A}\right)^2 \tag{S15}$$

$$\left(\frac{\Delta \bar{R}}{\bar{R}}\right)^2 = \left(\frac{\Delta N}{N}\right)^2 + \left(\frac{\Delta R}{R}\right)^2 \tag{S16}$$

$$\frac{\Delta L_c}{L_c} = \frac{1}{2}\left(\frac{\Delta N}{N}\right). \tag{S17}$$

6.2 Projected, Interfacial, and Apparent Wetted Area Ratios

The uncertainties in single droplet projected area, interfacial area, and apparent wetted area are given by

$$\left(\frac{\Delta A_{p,drop}}{A_{p,drop}}\right)^2 = 2\left(\frac{\Delta R}{R}\right)^2 \tag{S18}$$

$$(\Delta A_{i,drop})^2 = \left(\frac{\partial A_{i,drop}}{\partial R}\Delta R\right)^2 + \left(\frac{\partial A_{i,drop}}{\partial \theta}\Delta\theta\right)^2 \tag{S19}$$

$$(\Delta A_{w,drop})^2 = \left(\frac{\partial A_{w,drop}}{\partial R}\Delta R\right)^2 + \left(\frac{\partial A_{w,drop}}{\partial \theta}\Delta\theta\right)^2 \tag{S20}$$

where the partial derivatives are evaluated using Equations 10 and 11, with average values for radius and contact angle. The uncertainties in the cumulative area ratios are then given by

$$\left[\frac{\Delta(A_p/A)}{A_p/A}\right]^2 = \left(\frac{\Delta A_{p,drop}}{A_{p,drop}}\right)^2 + \left(\frac{\Delta A}{A}\right)^2 + \left(\frac{\Delta N}{N}\right)^2 \tag{S21}$$

$$\left[\frac{\Delta(A_i/A)}{A_i/A}\right]^2 = \left(\frac{\Delta A_{i,drop}}{A_{i,drop}}\right)^2 + \left(\frac{\Delta A}{A}\right)^2 + \left(\frac{\Delta N}{N}\right)^2 \tag{S22}$$

$$\left[\frac{\Delta(A_w/A)}{A_w/A}\right]^2 = \left(\frac{\Delta A_{w,drop}}{A_{w,drop}}\right)^2 + \left(\frac{\Delta A}{A}\right)^2 + \left(\frac{\Delta N}{N}\right)^2. \tag{S23}$$

6.3 Heat Flux and Heat Transfer Coefficient

Based on Equation 5, the uncertainty in single droplet heat transfer rate is estimated as

$$\left(\frac{\Delta \dot{q}_{drop}}{\dot{q}_{drop}}\right)^2 = \left(\frac{\Delta \rho}{\rho}\right)^2 + \left(\frac{\Delta h_{fg}}{h_{fg}}\right)^2 + 2\left(\frac{\Delta R}{R}\right)^2 + \left(\frac{\Delta (dR/dt)}{dR/dt}\right)^2 + \left(\frac{\Delta f}{f}\right)^2 \tag{S24}$$

with

$$f = \sin^3\theta \frac{d\theta}{dR} R + (1 - cos\,\theta)^2 (2 + cos\,\theta) \tag{S25}$$

where the contribution of water density and the latent heat of vaporization to the overall uncertainty was found to be negligible. Examination of Equation S9 shows that under the simplifying assumption of $C = 0.35 \approx 1/3$, the uncertainty in droplet growth rate is well approximated by

$$\frac{dR}{dt} \approx \frac{B^3}{3R^2} \qquad (C \approx 1/3) \tag{S26}$$

$$\left[\frac{\Delta (dR/dt)}{dR/dt}\right]^2 = 2\left(\frac{\Delta R}{R}\right)^2 + 3\left(\frac{\Delta B}{B}\right)^2 \tag{S27}$$

The uncertainty in the term f (given by Equation S25) is evaluated as

$$(\Delta f)^2 = \left(\frac{\partial f}{\partial \theta}\Delta\theta\right)^2 + \left(\frac{\partial f}{\partial R}\Delta R\right)^2 \tag{S28}$$

where the partial derivative terms are evaluated using average values for radius and contact angle. Finally, the uncertainty in total surface heat flux and the heat transfer coefficient can then be evaluated as

$$\left(\frac{\Delta \dot{Q}''}{\dot{Q}''}\right)^2 = \left(\frac{\Delta \dot{q}_{drop}}{\dot{q}_{drop}}\right)^2 + \left(\frac{\Delta A}{A}\right)^2 + \left(\frac{\Delta N}{N}\right)^2 \tag{S29}$$

and

$$\left(\frac{\Delta h_c}{h_c}\right)^2 = \left(\frac{\Delta \dot{Q}''}{\dot{Q}''}\right)^2 + \left(\frac{\Delta T_{sat}^i}{T_{sat}^i}\right)^2 \tag{S30}$$

where the uncertainty in interfacial saturation temperature difference is reported in Section 4.1.

References

(S1) Fraenkel-Conrat, H.; Williams, R. C. Reconstitution of active tobacco mosaic virus from its inactive protein and nucleic acid components. *Proc. Natl. Acad. Sci. U.S.A.* **1955,** *41* (10), 690-698.

(S2) Leapman, R. D.; Rizzo, N. W. Towards single atom analysis of biological structures. *Ultramicroscopy* **1999**, *78* (1–4), 251-268.

(S3) Lee, S.-Y.; Choi, J.; Royston, E.; Janes, D. B.; Culver, J. N.; Harris, M. T. Deposition of platinum clusters on surface-modified Tobacco mosaic virus. *J. Nanosci. Nanotechnol.* **2006**, 6 (4), 974-981.

(S4) Royston, E.; Ghosh, A.; Kofinas, P.; Harris, M. T.; Culver, J. N. Self-assembly of virus-structured high surface area nanomaterials and their application as battery electrodes. *Langmuir* **2007,** *24* (3), 906-912.

(S5) Laird, E. D.; Bose, R. K.; Wang, W.; Lau, K. K. S.; Li, C. Y. Carbon nanotube-directed polytetrafluoroethylene crystal growth via initiated chemical vapor deposition. *Macromol. Rapid Commun.* **2013,** *34* (3), 251-256.

(S6) Bose, R. K.; Nejati, S.; Stufflet, D. R.; Lau, K. K. S. Graft polymerization of anti-fouling PEO surfaces by liquid-free initiated chemical vapor deposition. *Macromolecules* **2012,** *45* (17), 6915-6922.

(S7) Nejati, S.; Lau, K. K. S. Pore filling of nanostructured electrodes in dye sensitized solar cells by initiated chemical vapor deposition. *Nano Lett.* **2010,** *11* (2), 419-423.

(S8) Bose, R. K.; Lau, K. K. S. Initiated CVD of poly(2-hydroxyethyl methacrylate) hydrogels: Synthesis, characterization and in-vitro biocompatibility. *Chem. Vap. Deposition* **2009,** *15* (4-6), 150-155.

(S9) Rykaczewski, K.; Scott, J. H. J.; Fedorov, A. G. Electron beam heating effects during environmental scanning electron microscopy imaging of water condensation on superhydrophobic surfaces. *Appl. Phys. Lett.* **2011,** *98*, 093106.

(S10) Enright, R.; Miljkovic, N.; Al-Obeidi, A.; Thompson, C. V.; Wang, E. N. Condensation on superhydrophobic surfaces: the role of local energy barriers and structure length scale. *Langmuir* **2012,** *28* (40), 14424-14432.

(S11) Atherton, T. J.; Kerbyson, D. J. Size invariant circle detection. *Image and Vision Computing* **1999**, *17* (11), 795-803.

(S12) Davies, E. R. Machine vision: Theory, algorithms, practicalities. 3rd Edition ed.; *Morgan Kauffman Publishers* **2005**.

(S13) Yuen, H. K.; Princen, J.; Illingworth, J.; Kittler, J. Comparative study of Hough Transform methods for circle finding. *Image and Vision Computing* **1990**, *8* (1), 71-77.

(S14) Carey, V. P. Liquid-vapor Phase-change Phenomena: An introduction to the thermophysics of vaporization and condensation processes in heat transfer equipment. *Hemisphere Publishing Corporation* **1992**.

(S15) Miljkovic, N.; Enright, R.; Wang, E. N. Effect of droplet morphology on growth dynamics and heat transfer during condensation on superhydrophobic nanostructured surfaces. *ACS Nano* **2012,** *6* (2), 1776-1785.

(S16) McCarthy, M.; Gerasopoulos, K.; Enright, R.; Culver, J. N.; Ghodssi, R.; Wang, E. N. Biotemplated hierarchical surfaces and the role of dual length scales on the repellency of impacting droplets. *Appl. Phys. Lett.* **2012,** *100*, 263701.

(S17) Miljkovic, N.; Enright, R.; Wang, E. N. Modeling and Optimization of Superhydrophobic Condensation. *J Heat Trans-T Asme* **2013,** 135, (11), 111004.

(S18) Abu-Orabi, M. Modeling of heat transfer in dropwise condensation. *Int J Heat Mass Tran* **1998,** 41, (1), 81-87.

(S19) Kim, S.; Kim, K. J. Dropwise Condensation Modeling Suitable for Superhydrophobic Surfaces. *J Heat Trans-T Asme* **2011,** 133, (8), 081502.